Combustion Efficiencies and Flameout Limits Computed for a Hypersonic Vehicle During Ascent

Chukwuka C. Mbagwu* and James F. Driscoll†
University of Michigan, Ann Arbor, Michigan 48109
Derek J. Dalle‡
NASA Ames Research Center, Moffett Field, California 94035
and
Sean M. Torrez§
Physical Sciences, Inc., Andover, Masachusetts 01810

DOI: 10.2514/1.B36479

Computations were performed to understand propulsion tradeoffs that occur when a hypersonic vehicle travels along an ascent trajectory. Operability limits are plotted that define allowable flight corridors on an altitude versus flight Mach number performance map. Two operability limits are set by requirements that combustion efficiency exceeds 0.90 and that flameout be avoided. Ambient gas pressure decreases during ascent, which for a fixed waverider inlet (compressor) design slows finite rate chemistry in the combustor. However, this can be offset by increases in flight Mach number and gas temperature in the combustor. New aspects of the work are that operability limits are computed for a waverider trimmed at each altitude. The University of Michigan–U.S. Air Force Research Laboratory scramjet in vehicle waverider model includes finite rate chemistry, three-dimensional mixing, ram–scram transition, and an empirical value of the flameout Damköhler number. A reduced-order modeling approach is justified (instead of computational fluid dynamics results) because all vehicle forces are computed over 1800 times to generate multidimensional performance maps. Trajectories were optimized to achieve highest combustion efficiency and avoid flameout limits.

I. Introduction

THERE are several interesting tradeoffs that occur when a hypersonic waverider ascends along a trajectory of constant dynamic pressure ($q = 1/2\rho_\infty U_\infty^2$). Figure 1 shows the geometry of the MAX-1 waverider that the authors have analyzed [1–9] using their reduced-order model called the University of Michigan–U.S. Air Force Research Laboratory scramjet in vehicle (MASIV). A constant-q trajectory might be selected from one of the three solid curves in Fig. 2, which is a flight corridor map of altitude versus flight Mach number. The unstart limit that is shown was computed in [2]; it occurs when the combustor applies an excessively high backpressure on the shock train in the engine isolator, forcing the shocks to move upstream and creating unwanted spillage. The low and high ambient pressure operability limits are described in Sec. V. Two operability limits of interest are the flame instability or flameout limit, a hard constraint, and the loose requirement of maintaining a high combustion efficiency greater than 90%. The second requirement is flexible in that operating at lower efficiency is feasible but leads to excess fuel burn and reduced range. A desired trajectory is one that avoids crossing these two limits. Computations of these operability limits have not been reported previously; to do so, our reduced-order model [1–9] had to be improved using the approach described in Sec. IV.

During the vehicle ascent, the ambient static pressure drops, creating low-pressure conditions that reduce the chemical reaction rates in the combustor, despite the initial inlet compression. Ambient static temperature does not vary as significantly by comparison. Another undesirable effect is that the airflow velocity in the combustor increases, reducing the residence time available to complete combustion. However, the vehicle accelerates along the ascent trajectory, increasing the flight Mach number and oblique shock strength. Because ambient static temperature remains relatively constant (small relative rise), this then increases the static temperature entering the combustor after the shock train and tends to speed up the finite rate chemistry. Figure 3 illustrates the inverse trends of static pressure and temperature with increasing altitude.

Another complication is that the fuel–air equivalence ratio (ER) varies in a different way along each trajectory, and it cannot be specified a priori. ER is determined by two factors: the thrust that is required to "trim" the vehicle, and the entrained air mass flow rate. Trimming the vehicle is an iterative process by which a vehicle configuration is computed that balances the aerodynamic and propulsive forces such that a given flight condition (Mach number, acceleration, and altitude) is met. The equivalence ratio, angle of attack, and control surface deflections are independent parameters that constitute the vehicle configuration; they are varied until the flight condition is matched within tolerance. Thrust depends on the vehicle drag and angle of attack, which in turn depends on the vehicle weight. The engine air mass flow rate is $\rho_\infty U_\infty A_c$, and this can be rewritten as $(2q\rho_\infty)^{1/2}A_c$, where A_c is the capture area. Selecting a large dynamic pressure q trajectory will tend to increase the air mass flow rate and reduce the required ER for trim. However, this relation shows that, during ascent, the air mass flow rate drops due to the low gas density at high altitudes, which tends to increase the ER necessary to meet the target flight condition, including the target acceleration. Because of these complex tradeoffs, a model can help to understand how ER, pressure, temperature, and gas velocity in the combustor can affect the combustion efficiency and the flameout limit.

One of the operability limits of interest corresponds to the requirement that combustion efficiency η_C exceeds 0.90. Heiser et al. [10] define η_C to be

$$\eta_C = \frac{\dot{m}_{H2,\text{burned}}}{\dot{m}_{H2,\text{inj}}} = \frac{\dot{m}_{H2,\text{inj}} - \dot{m}_{H2,4}}{\dot{m}_{H2,\text{inj}}} \tag{1}$$

Received 20 September 2016; revision received 16 August 2017; accepted for publication 21 August 2017; published online 23 November 2017.

*Graduate Researcher, Department of Aerospace Engineering; cmbagwu@umich.edu. Senior Member AIAA.
†Professor, Department of Aerospace Engineering; jamesfd@umich.edu. Fellow AIAA.
‡Research Scientist, MS 258-2. Member AIAA.
§Principal Engineer. Member AIAA.

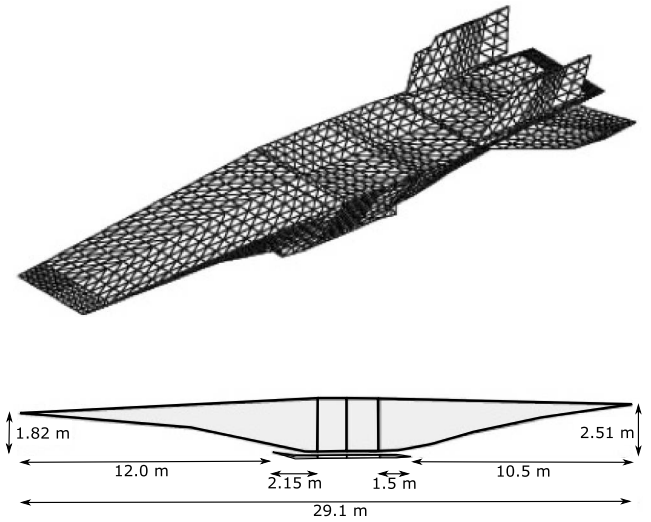

Fig. 1 MAX-1 hypersonic waverider vehicle. Engine width is 2.143 m. For details, see [3,4].

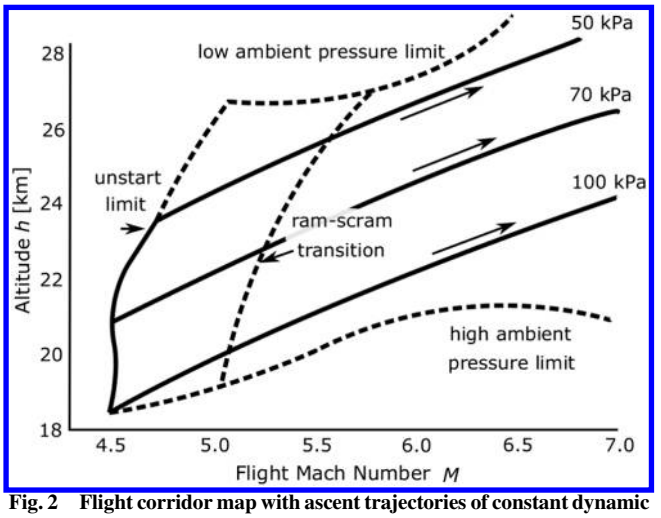

Fig. 2 Flight corridor map with ascent trajectories of constant dynamic pressure. Unstart and ram-scram limits are from [2]. Low and high pressure limits depend on flameout and combustion efficiency.

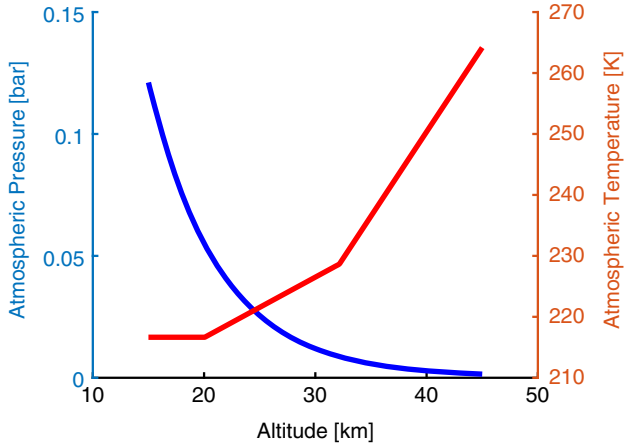

Fig. 3 Atmospheric conditions for pressure p_∞ (left) and temperature T_∞ (right) as a function of altitude.

where $\dot{m}_{H2,\text{inj}}$ is the mass flow rate of the hydrogen fuel that is injected from wall ports. The quantity $\dot{m}_{H2,4}$ is the mass flow rate of unburned hydrogen that passes through the combustor exit. Stations 3 and 4 are defined to be the entrance and exit of the combustor, respectively, as drawn in Fig. 1.

The second operability limit of interest is the flameout limit [10–15]. Flameout occurs when the air velocity at the entrance to the combustor (U_3) exceeds the critical air velocity (U_3^*) that is determined by setting the normalized Damköhler number Da_H equal to 1. The Damköhler number criterion was pioneered by Ozawa [13] and has been validated in many studies, including recent advances by Shanbhogue et al. [14] and Driscoll and Rasmussen [12]. Damköhler number Da is defined as the ratio of the fluid mechanical time to a chemical time τ:

$$Da = \frac{S_L^2/\alpha}{U/H} \approx \frac{\text{reaction rate } \omega_\tau}{\text{diffusion rate}} \tag{2}$$

where S_L is the laminar burning velocity, and α is the thermal diffusivity. The inverse of the numerator in Eq. (2) is the chemical time τ, which is correlated to a maximum fuel reaction rate $\omega_\tau \approx 1/\tau$. For $Da \gg 1$, the reaction rate is much greater than diffusion, and the steady solution is said to be diffusion-limited. For $Da \ll 1$, diffusion occurs much faster than the reaction.

The Damköhler number is computed for a number of experiments with cavity flameholders in a high-speed crossflow. These experiments [16–20] measured flame stability under various flow conditions and cavity configurations at or immediately before flame blowout. Critical Damköhler number and reaction rate, Da^*_{crit} and ω^*_τ, are computed in the MASIV combustor reduced-order model (ROM) from the given experimental conditions.

We define the normalized Damköhler number Da_H to be

$$Da_H = \frac{\omega_\tau/(U_3/H)}{[\omega^*_\tau/(U^*/H)]_{\text{flameout}}} = \frac{\omega_\tau/(U_3/H)}{Da^*_{\text{crit}}} \tag{3}$$

such that $Da_H = 1$ at a critical or flameout Damköhler number. Above this value, Da_H represents a stable flame, whereas $Da_H < 1$ signals flameout.

ω_τ is the maximum reaction rate of the fuel inverse seconds. It depends on the equivalence ratio (ER), static pressure p_3, and static temperature T_3 at the combustor entrance. Similar to previous studies [16–25], it is assumed that a wall-cavity flame holder is used, and so the characteristic length scale is the height H of the wall-cavity. The recirculating flow in the wall-cavity is not explicitly modeled in MASIV. Equation (3) is rearranged to state that the critical air velocity U_3 at the flameout limit ($Da_H = 1$) is

$$U_3^* = k_1 H \omega_\tau \tag{4}$$

The constant k_1 in Eq. (4) is another way of representing the denominator of Eq. (3). Constant k_1 must be determined from experimental data because computational fluid dynamics (CFD) computations cannot reliably compute a flameout limit. Fortunately, there are many measured values of flameout limits for cavity flame holders that provide values of k_1. Measurements of Takahashi et al. [16] were selected because their flameout limit was recorded for a scramjet experiment that was operated on hydrogen fuel with a cavity flame holder. They measured a flameout velocity U_3^* at 1336 m/s for a cavity height H of 0.36 cm. Their static temperature T_3 and pressure p_3 were 1111 K and 0.47 bar, respectively. From these values, their reaction rate ω_τ^* is computed by the MASIV code. The resulting value of constant $k_1 = 2893$ for Takahashi et al. [16], and this was used in our analysis. Table 1 lists other experiments with reported values of U_3^* and Da^*_{crit} that could be used instead of those of Takahashi et al.

There are several goals of the present study. Two cases were defined; the first is called the assessment case, and the second is the ascent case. For the assessment case, the vehicle does not ascend, and three of the four parameters [p_3, T_3, U_3, and ER] are fixed. Initially, p_3 is varied alone, and later T_3 is varied alone, and two quantities are computed: combustion efficiency and Damköhler number. The results help to understand the relative role of pressure and

Table 1 Measured air velocity and Damköhler number at flameout for hydrogen–air experiments

Authors	Fuel	Critical velocity U_3^*, m/s	$Da_{\text{crit}}^*(\times 100)$	ω_τ^*, 1/s
Takahashi et al. [16]	H_2	1336	0.03456	128.29
Sun et al. [17]	H_2	991	0.13757	170.48
Micka and Driscoll [18]	H_2	487	3.9066	1498.03
Kang et al. [19]	H_2	1707	0.15051	856.63
Retaureau and Menon [20]	H_2	1100	0.13855	60.002

temperature. In contrast, for the ascent case, all four of these parameters vary as the vehicle ascends along a constant dynamic pressure trajectory, with a fixed vehicle acceleration. Trim conditions are imposed at several different altitudes along each of the nine trajectories (i.e., values of dynamic pressure). At each altitude, the forces and moments are computed at multiple angles of attack to determine the angle and fuel–air ratio that trims the vehicle. Along each trajectory, the altitude is recorded where flameout occurs and where η_C drops below 0.90. Results are stored in a multidimensional matrix used to plot operability limits and determine a trajectory that maximizes combustion efficiency while avoiding the aforementioned limits.

II. Motivation for Reduced-Order Models

The study of hypersonic vehicles poses unique challenges in that the engine is tightly coupled with the vehicle, and so it is not possible to analyze the engine by itself. Combustor pressure should not be allowed to drop too low, and so the oblique shock pattern in the inlet and isolator must be strong enough to provide sufficient compression. The inlet shock strength depends on the vehicle angle of attack. This angle is determined by the trim condition that thrust, drag, and acceleration be properly balanced. However, the thrust depends on the combustor pressure, temperature, and other engine conditions, and so these parameters are interrelated. As such, solutions can only be found through an iterative process. A second obstacle is that, to create the necessary trajectory surface maps, more than 1800 "runs" or full-vehicle computations, including the engine, had to be made. Each run computes the vehicle forces and moments as well as the axial profiles of static pressure and temperature in the engine: across the inlet shocks, the isolator, the combustor, and the exhaust nozzle. One approach might be to perform high-fidelity CFD simulations of the entire hypersonic vehicle, including the engine flowpath, for the more than 1800 run conditions. However, this requires excessive computational cost and time. Another approach is to gain an approximate understanding of the solution through a reduced-order model (ROM) that provides a "first look" at a large multidimensional parameter space.

Previously, the advantages of ROMs have been pointed out by U.S. Air Force Research Laboratory (AFRL) researchers Bolender and Doman [26], O'Neill and Lewis [27], O'Brien et al. [28], Bowcutt [29] at Boeing, Dalle et al. [1–3], Torrez et al. [4,5], Mbagwu and Driscoll [6], Lamorte et al. [7], Mbagwu and Driscoll [8,9], and Chavez and Schmidt [30]. The Bolender–Doman AFRL ROM was developed in 2006 [26] to simulate the flight dynamics, poles, and zeros of a hypersonic vehicle. This early ROM relied on additional assumptions. Forces on each surface panel were computed using a hypersonic panel method that assumes small angle deflections, no flow separation, and no detached bow shock wave. Viscous forces were estimated using hypersonic flat-plate approximations. Compression by the bow shock was computed, but internal shock waves were ignored. The combustor was a constant-area duct with effective heat addition due to combustion, and the combustion was assumed to be fast and 100% completed within the available combustor length.

To improve on the Bolender–Doman AFRL analysis, a second-generation model, called MASIV (from "Michigan–AFRL scramjet in vehicle") was developed during a joint collaboration between the University of Michigan and AFRL [1–9], some details of which are summarized in Sec. III. Items that were added include multiple interacting shock waves in the two-dimensional (2-D) inlet (and the exhaust nozzle) using a technique similar to the method of characteristics. In the combustor, three-dimensional (3-D) fuel–air mixing was added by assuming that a wall jet issues from N wall ports. Empirical formulas were obtained from experimental data that describe the fuel concentration profiles within each fuel jet [31]. Finite rate chemistry was added by including a strained flamelet chemistry lookup table computed from the Stanford FlameMaster code.

Using the MASIV model, one run requires less than 1 min of computational time on a single processor. ROMs have proven useful in this regard when the goal is to optimize the geometry, the trajectory, or the control of the vehicle system. The shorter computational time also allows ROMs to quickly generate solutions over a wide parameter space and identify areas of interest that then guide the judicious use of CFD for a smaller subset of conditions where higher accuracy is desired. Thus, ROMs do not compete with high-fidelity CFD but rather can be used alongside CFD to efficiently characterize and analyze large, multidimensional parameter spaces. The performance of MASIV has previously been validated against commercial CFD codes [2,4].

III. Reduced-Order Model

This section details the reduced-order model for the MAX-1 waverider vehicle that is drawn in Fig. 1, with emphasis on the combustor and jet-in-crossflow formulation. The vehicle is similar to the generic aircraft that was first considered at AFRL by Bolender and Doman [26]. It has a length of 29.1 m (95.4 ft), and the width of the dual mode ramjet–scramjet engine is 2.143 m. The inlet is rectangular with a sufficiently large aspect ratio of 15.3 such that it can be considered to be two-dimensional. The isolator is 1.38 m long and is followed by the constant-area portion of the combustor that is 0.90 m long; both have a cross section of 0.14 by 2.143 m. The second part of the combustor is 0.62 m long, and its upper wall diverges at 4 deg.

Forces on each surface panel are computed using a small-angle panel method, and the method to trim the vehicle is described in [1,2]. The engine inlet is drawn in Fig. 4, and it contains multiple shock waves that interact. The inlet code is similar to the method of characteristics, and it computes the static pressure rise and the stagnation pressure loss in the inlet. It assumes that the flow is 2-D, wall deflection angles are small, no flow separation occurs, and the supersonic inlet Mach number is small enough that strong shock/boundary-layer interactions do not occur.

The MASIV combustor submodel was described in detail in [1–9], and so only a summary is provided here. The code includes finite rate chemistry, real gas properties, a three-dimensional jet mixing model, a separated boundary-layer model, and gas dissociation. The airstream is modeled as the one-dimensional (1-D) flow in the duct that is drawn in Fig. 5. It has variable area, friction, wall heat transfer,

Table 2 Combustor entrance conditions for the cavity-stabilized hydrogen–air scramjet experiments

Authors	Fuel	Temperature T_3, K	Pressure p_3, bar	Cavity step height H, m	Equivalence ratio (ER)
Takahashi et al. [16]	H_2	1111	0.47	0.0036	0.30
Sun et al. [17]	H_2	823	1.01	0.0080	0.40
Micka and Driscoll [18]	H_2	1390	0.50	0.0127	0.30
Kang et al. [19]	H_2	1570	1.32	0.0030	0.18
Retaureau and Menon [20]	H_2	410	0.65	0.0254	0.25

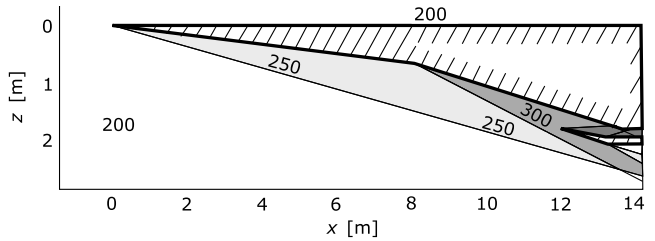

Fig. 4 Shock and temperature (in kelvins) contours of the MAX-1 vehicle trimmed at Mach 8, computed in [2].

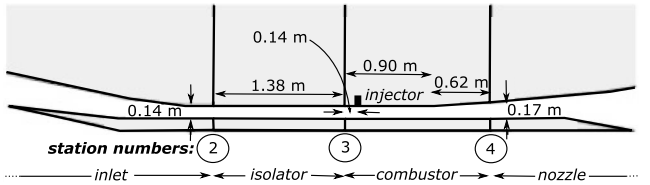

Fig. 5 Dual-mode ramjet–scramjet internal flowpath of the MAX-1 waverider.

and heat addition due to combustion. Fuel is injected from $N = 19$ ports that are located at one x location that is 0.14 m downstream of station 3, as shown in Fig. 5. The 19 fuel jets are located at different spanwise locations across the 2.143 m width; each port is 3.45 cm in diameter. Each port is choked, and the hydrogen fuel enters at 300 K and at the sonic speed of 1295 m/s.

MASIV solves the following seven ordinary differential equations, which include the conservation of mass [Eq. (5)], momentum [Eq. (6)], energy [Eq. (10)], and species [Eq. (11)]. The equations are derived in [4,27]:

$$\frac{1}{\rho}\frac{d\rho}{dx} = \frac{1}{\dot{m}}\frac{d\dot{m}}{dx} - \frac{1}{u}\frac{du}{dx} - \frac{1}{A}\frac{dA}{dx} \tag{5}$$

$$\frac{1}{u}\frac{du}{dx} = -\frac{1}{\rho u^2}\frac{dp}{dx} - \frac{2c_f}{D} + \left(1 - \frac{u_F}{u}\right)\frac{1}{\dot{m}}\frac{d\dot{m}}{dx} \tag{6}$$

$$\frac{1}{p}\frac{dp}{dx} = \frac{1}{\rho}\frac{d\rho}{dx} + \frac{1}{T}\frac{dT}{dx} - \frac{1}{W}\frac{dW}{dx} \tag{7}$$

$$\frac{1}{W}\frac{dW}{dx} = -\sum_{i=1}^{n_{sp}}\frac{W}{W_i}\frac{dY_i}{dx} \tag{8}$$

$$\frac{d\dot{m}}{dx} = \sum_{i=1}^{n_{sp}}\frac{d\dot{m}_{i,F}}{dx} \tag{9}$$

$$c_p\frac{dT}{dx} = \frac{h_{0,F} - h_0}{\dot{m}}\frac{d\dot{m}}{dx} - \frac{2c_f c_p(T_{aw} - T_w)}{Pr^{2/3}D} - u\frac{du}{dx} - \sum_{i=1}^{n_{sp}} h_i\frac{dY_i}{dx} \tag{10}$$

$$\frac{dY_i}{dx} = \frac{\bar{\omega}_i W_i A}{\dot{m}} + \frac{1}{\dot{m}}\frac{d\dot{m}_{i,F}}{dx} - \frac{Y_i}{\dot{m}}\frac{d\dot{m}}{dx} \tag{11}$$

Equations (7) and (8) define the equation of state and the molecular weight W of the gas mixture, respectively. Equation (9) states that the total mass flow rate is that of the component species of the oxidizer (air), fuel (hydrogen), and other intermediate species. Note that the fuel is injected at a single x location, downstream of the combustor entrance.

An important quantity is the volumetric reaction rate of each species ($\bar{\omega}_i$) that appears in Eq. (11) within the first term on the right side. This reaction rate controls how the mass fraction of each species (Y_i) varies in the x direction. The overbar denotes that $\bar{\omega}_i$ has been averaged over the y and z directions, and so it is only a function of the streamwise coordinate x. The reaction rate depends on two submodels: an empirical model for the 3-D fuel–air mixing of a jet in crossflow, and a submodel of the finite rate chemical reactions. Both are described in detail in Torrez et al. [4]. A spatial representation of the spreading profile for a jet in crossflow is shown in Fig. 6.

The model geometry is limited to one specific configuration: that of N independent fuel jets at a single axial location injected into a crossflow of air. Empirical formulas [Eqs. (12–19)] that define the fuel jet spreading and mixing were validated by the experiments of Hasselbrink and Mungal al. [31,32] and Smith and Mungal [33]. The centerline of each fuel jet bends over such that its y coordinate (y_C) is related to its x coordinate (x_C) according to [31,33]

$$r_u = \left[\frac{\rho_F}{\rho_A}\left(\frac{U_F}{U_A}\right)^2\right]^{1/2}$$
$$\frac{y_C}{d_F} = c_1\left(\frac{x_C}{d_F}\right)^{c_2} r_u^{2/3} \tag{12}$$

where d_F is the fuel jet diameter, and r_u is the fuel jet momentum ratio. The decay of the time-averaged, normalized fuel mass concentration ξ_C along the centerline is given by the far-field scaling law [32,33]:

$$\xi_C = c_3\left[\frac{\rho_F}{\rho_A}\left(\frac{U_F}{U_A}\right)^{-1}\left(\frac{x_C}{d_F}\right)^{-2}\right]^{1/3} \tag{13}$$

The mean mixture fraction along the centerline $\tilde{f}_C$ is then correlated to the concentration ξ_C and is assumed to be unity in the injected fuel stream and zero in the upstream crossflow:

$$\tilde{f}_C = \frac{\xi_C(W_F/W_A)}{1 + ((W_F/W_A) - 1)\xi_C} \tag{14}$$

where W is the molecular weight of the fuel or oxidizer. The mixture fraction at any point in the flowfield $\tilde{f}$ can be computed by mapping the shortest distance from that point to the jet centerline. Smith and Mungal [33] showed that the resultant mixture fraction $\tilde{f}(s, n)$ has a Gaussian profile in the direction normal to the curved jet centerline and is dependent on the radial jet spreading distance b, a function of the distance along the centerline (s), and the perpendicular distance from the centerline (n):

$$n^2 = (x - x_C)^2 + (y - y_C)^2 + z^2$$
$$\frac{b}{d_F} = c_4 r_u^{2/3}\left(\frac{x_C}{d_F}\right)^{c_2}$$
$$\tilde{f}(s, n) = \tilde{f}_C \exp\left(\frac{-n^2}{2b^2}\right) \tag{15}$$

The variance of the mixture fraction $\widetilde{f''^2}$ is a function of the gradient of the mean mixture fraction, according to the Prandtl mixing length relation:

$$\sqrt{\widetilde{f''^2}} = \frac{c_5}{c_4} b|\nabla\tilde{f}| \tag{16}$$

Following this, the mean scalar dissipation rate $\tilde{\chi}$ is given by the following formula, where D_T is the turbulent scalar diffusion coeficient, modeled by a relation of the turbulent kinematic viscosity ν_T and the turbulent Schmidt number ($Sc_T = 0.7$):

$$\tilde{\chi} = 2D_T|\nabla\tilde{f}|^2 \tag{17}$$

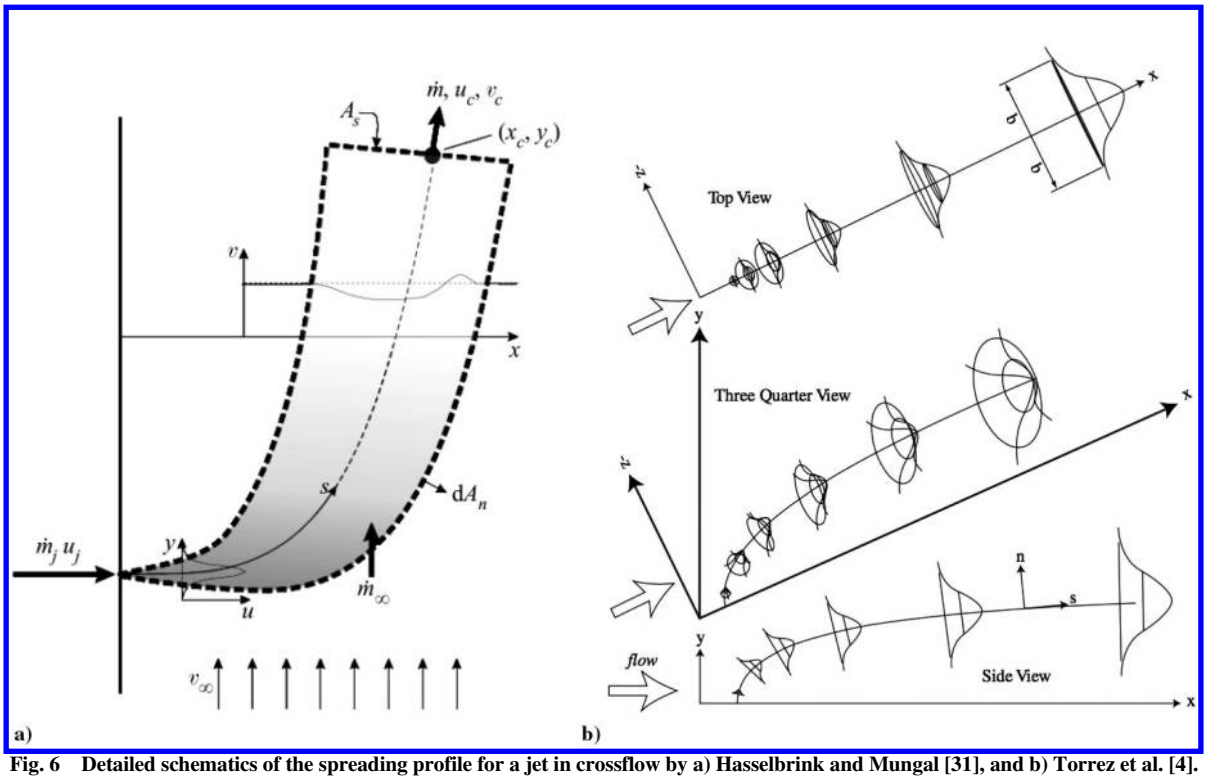

Fig. 6 Detailed schematics of the spreading profile for a jet in crossflow by a) Hasselbrink and Mungal [31], and b) Torrez et al. [4].

$$D_T = \frac{\nu_T}{Sc_T} \tag{18}$$

$$U_F d_F/\nu_T = c_6 \tag{19}$$

These relations determine how the flow mixture properties vary spatially in a three-dimensional field where a fuel jet progresses along its centerline. In particular, the flowfield mixture fraction $\tilde{f}$, variance $\widetilde{f''^2}$, and the scalar dissipation rate $\tilde{\chi}$ from Eqs. (15–17), along with local combustor pressure and temperature conditions derived from Eqs. (5–11), are necessary to compute the volumetric reaction rate $\bar{\omega}_i$ from the chemical kinetic flamelet tables. Using a flamelet model, the reaction rate of each species is then

$$\dot{\omega}(x, y, z) = \dot{\omega}\left(\tilde{f}, \widetilde{f''^2}, \tilde{\chi}(f), p, T\right) \tag{20}$$

The profiles of the mixture properties are matched empirically to low-speed experiments, giving rise to the values of constants c_1 to c_5, which are used in this study. Recent investigations [5,34] have found similar scaling relations for transonic and supersonic flows, and so their use here is appropriate. The quantity $U_F d_F/\nu_T$ is taken as a tunable parameter in the model, and c_6 is chosen to correlate with additional mixing suppression due to the high-speed flow.

IV. New Additions to the MASIV Model to Improve the Finite Rate Chemistry

To achieve the current goals of computing combustion efficiency and flameout limits, two major additions were made to the MASIV model: the chemistry lookup table was extended to the low pressures associated with high-altitude flight, and an advanced interpolation method based on proper orthogonal decomposition (POD) was added. Finite rate chemistry is included by using a flamelet approach, similar to that of Ihme and See [35] and Peters [36]. A flamelet lookup table was generated with the Stanford FlameMaster code [35,37] that solves flamelet equations. For example, a flamelet equation for hydrogen species relates the mixture fraction dissipation rate, diffusion of H_2 mass fraction in mixture fraction space, and the H_2 reaction rate in the following way:

$$\frac{-\chi}{2}\frac{\partial^2 Y_{H2}}{\partial Z^2} = \dot{\omega}_{H2} \tag{21}$$

The reaction rate on the right side of Eq. (21) was computed for eight species (H_2, O_2, H_2O, H, OH, O, HO_2, and H_2O_2) and 24 elementary reactions [38]. A chemistry lookup table was generated that correspond to four discrete combustor entrance static pressures p_3 of 0.1, 0.32, 1.0, and 3.16 bar and four combustor entrance static temperatures T_3 of 500, 900, 1300, and 1700 K.

Equations (12–21) yield 3-D contours of the hydrogen reaction rate $\dot{\omega}_{H2}$ downstream of each of the 30 wall jets that are drawn in Fig. 7. Figure 8a shows some 2-D slices of the computed 3-D profiles. Reaction rate in the upper profile of Fig. 8a is largest just downstream of the wall fuel port, where scalar gradients are large. Reaction rates are smaller for the case of lower static pressure (Fig. 8a, lower profile) because the low pressure reduces the Arrhenius reaction rate as well as the fuel–air mixing rate. A mixing and jet scaling model is used for these computations, detailed in [4,33], and the MASIV model further solves Eqs. (5–11).

Figure 8b contains plots of the integrated hydrogen reaction rate $\overline{\dot{\omega}_{H2}}$. The profiles in Fig. 8b were integrated over each transverse (y, z) plane, using

$$\overline{\dot{\omega}_{H2}}(x) = \frac{1}{A}\iint \dot{\omega}_{H2}(x, y, z)\, \mathrm{d}y\, \mathrm{d}z \tag{22}$$

Thus, the integrated hydrogen reaction rate $\overline{\dot{\omega}_{H2}}$ plotted in Fig. 8b is only a function of the streamwise coordinate x. This integrated reaction rate is required as input into Eq. (11), which determines how

Table 3 Experimental constants for jet mixing model, tabulated in [4]

Constant	Experimental range	MASIV value
c_1	1.2–2.6 [32]	1.6
c_2	0.28–0.34 [32]	1/3
c_3	0.68–0.95 [33]	1.3
c_4	0.76 [32]	0.76
c_5	0.0084–0.0093 [33]	0.009
c_6	— —	15

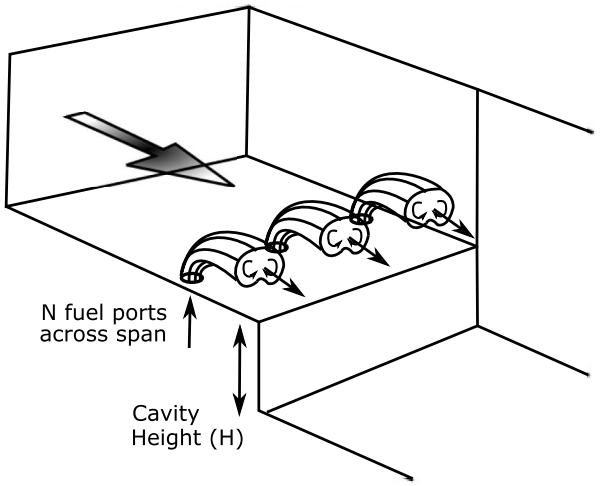

Fig. 7 Schematic of fuel ports and fuel jets across the span of the combustor. Also marked is the height H of the flame holder cavity.

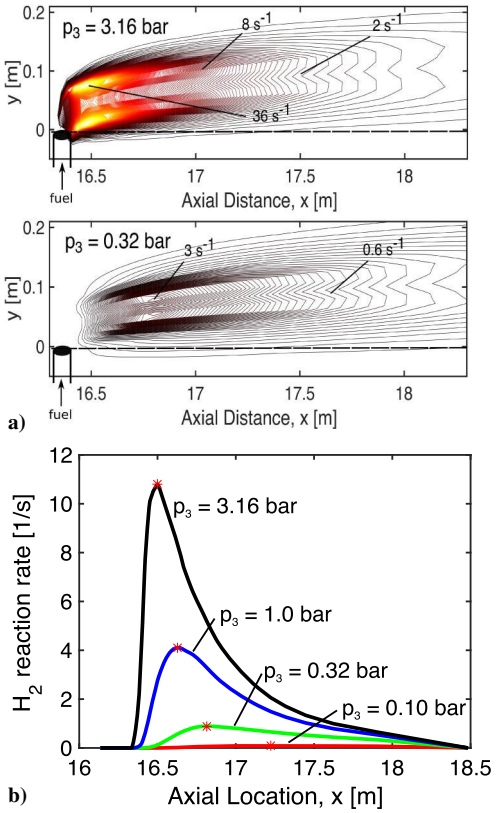

Fig. 8 Top: 2-D slices of 3-D contours of hydrogen reaction rate within a fuel jet; bottom: 1-D profiles of reaction rate by integrating contours over y–z planes.

rapidly the hydrogen fuel was consumed in the flow direction downstream of the fuel port.

The curve marked $p_3 = 3.16$ bar in Fig. 8b represents the highest pressure in this figure, and the peak reaction rate is seen to be much larger than for the lowest-pressure condition (0.1 bar). The trend in Fig. 8b confirms the general rule that compression in the inlet should be sufficient to maintain combustor pressure above some baseline value, which is stated in Heiser et al. [10] to be about 0.5 atm.

A quantity of interest is the maximum fuel reaction rate ω_τ, used in Eq. (4) to compute the air velocity at the flameout limit (U_3^*). This reaction rate is given by

$$\omega_\tau = \frac{[\dot{\omega}_{H2}(x,y,z)]_{\max}}{\rho_{H2}} \tag{23}$$

$$\rho_{H2} = \frac{\dot{m}_{H2}}{(U_{H2}\pi d_F^2/4)} \tag{24}$$

The first factor on the right $[\dot{\omega}_{H2}(x,y,z)]_{\max}$ corresponds to the maximum values of the contours drawn in Fig. 8. The density of the injected hydrogen (ρ_{H2}) depends on the equivalence ratio ER, which determines the mass flow rate of hydrogen via the following relation: $(\dot{m}_{\text{fuel}}/\dot{m}_{\text{air}})/f_s$. Here, f_s is the stoichiometric fuel–air ratio, which is 0.029 for hydrogen. The hydrogen injection velocity U_{H2} is the sonic velocity of hydrogen (1200 m/s) at 300 K. The diameter of each fuel port (d_F) on the MAX-1 vehicle is 3.45 cm.

Combustion efficiency was defined in Eq. (1) to be the fraction of the total mass flow rate of hydrogen that is consumed in the combustor. The unburned hydrogen mass flow rate $\dot{m}_{H2,4}$ in the equation is replaced with $Y_{H2,4}\dot{m}_4$, where $Y_{H2,4}$ is the mass fraction of hydrogen at the combustor exit. The exit mass flow rate $\dot{m}_4$ is replaced with $\dot{m}_3 + \dot{m}_{H2,\text{inj}}$, where $\dot{m}_3$ is the entering air mass flow rate. The fuel–air equivalence ratio (ER) is defined to be

$$\text{ER} = \frac{\dot{m}_{H2,\text{inj}}}{\dot{m}_3 f_s} \tag{25}$$

When the preceding relations are substituted into Eq. (1), the combustion efficiency becomes

$$\eta_C = 1 - \left(\frac{Y_{H2,4}}{f_s \text{ER}}\right)(1 + f_s \text{ER}) \tag{26}$$

At each altitude during the ascent, the combustor entrance pressure and temperature are computed as well as the mass fraction of hydrogen at the combustor exit ($Y_{H2,4}$). This quantity is substituted into Eq. (26), along with the ER required to trim the vehicle, to compute the combustion efficiency.

The flameout limit was computed by employing Eqs. (2) and (4). First, a cavity flame holder of height H is selected for the MAX-1 vehicle. At each altitude along a constant dynamic pressure q_∞ trajectory, the vehicle is trimmed to compute the angle of attack and equivalence ratio required to produce the necessary thrust. Then, MASIV computes the values of $\omega_\tau/\omega_\tau^*$ and U_3 at each altitude. ω_τ is the reaction rate of the fuel for the pressure and temperature at the combustor entrance. ω_τ^* is computed in the same way, but for the measured pressure and temperature at flameout of the Takahashi et al. [16] experiment. These values are input into Eqs. (2) and (4), and if the computed air velocity U_3 exceeds the critical value U_3^*, then flameout is predicted to occur.

A new method was developed to reduce the computational time of the model and improve the interpolation between discrete values in the lookup table. First, a large lookup table was filled with computed values of chemical reaction rates. Second, the size of the table is reduced to less than 1% of its original size through a matrix decomposition of the data tables. Additionally, most of the table elements have negligibly small values of reaction rate. The third step was to apply a rapid interpolation method because the combustor inlet pressure and temperature (p_3, T_3) at each altitude will fall in between the 16 discrete values that were used to compute the lookup table. Standard interpolation methods were found to be too slow or too inaccurate to handle the multidimensional and occasionally ill-conditioned lookup tables.

Proper orthogonal decomposition (POD) is a well-defined method of producing reduced models of complex data sets. In this application, it provides a rapid and accurate way to reduce the size of the lookup table and enable rapid interpolation. The POD method represents the data approximately using a linear combination of basis functions, and only the modes that make the largest contributions are retained. POD methods, as described in [39–41], are analogous to

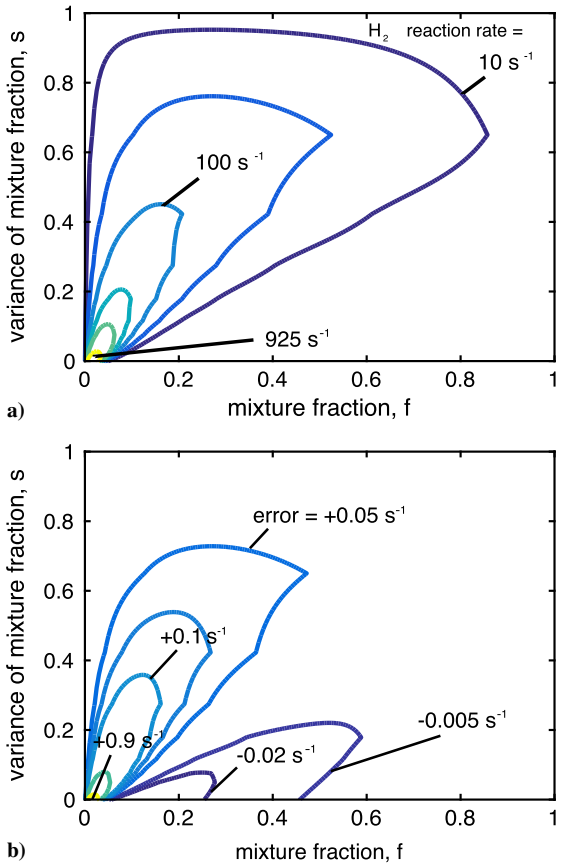

Fig. 9 Representations of a) Contours of hydrogen reaction rate for one flamelet. Dissipation rate $\chi = 882$ s^{-1}, $p_3 = 3.16$ bar, $T_3 = 1300$ K; b) POD truncation errors of less than 1%.

representing a time-varying voltage as a function of sine and cosine basis functions, along with their associated Fourier coefficients.

The lookup table for the finite rate chemistry is a multidimensional matrix that is called $\boldsymbol{S}$. It contains 93,907,200 elements; each element is a chemical reaction rate that was computed by solving the flamelet Eq. (21) using the Stanford FlameMaster code. This code considers 24 elementary reactions and eight species (H_2, O_2, H_2O, H, OH, O, HO_2, and H_2O_2) from the Jachimowski mechanism [38]. The large number of elements in $\boldsymbol{S}$ is the product of six parameters; reaction rates are tabulated for each of the eight species for four values of p_3 and 4 values of T_3. For good accuracy, it was decided to consider 201 values of mean mixture fraction, 25 scalar variances, and 146 scalar dissipation rates.

Figure 9a displays some of the reaction rates stored in $\boldsymbol{S}$ for one scalar dissipation rate of 882 s^{-1}. Hydrogen (H_2) reaction rate is plotted as a function of mean mixture fraction and its variance. Notice that there is a small region in the bottom left where the reaction rates are significant (above 900 s^{-1}).

At most of the other locations in Fig. 9a, reaction rates are less than 5% of this value. Therefore, a new smaller matrix called $\tilde{\boldsymbol{S}}$ then is computed that retains only the small number of significant reaction rates that are seen in the lower-left corner of Fig. 9. Many elements are ignored for which reaction rate is nearly zero. The new matrix $\tilde{\boldsymbol{S}}$ has less than 1% as many elements as $\boldsymbol{S}$. To identify and reduce the matrix $\boldsymbol{S}$, a POD decomposition is performed, and only the four largest POD modes are retained. A more complete formulation of this POD approach and its accuracy is detailed in [8].

V. Results

We consider two cases; one is the assessment case, and the other is the ascent case. For the assessment case, there is no ascent of the vehicle, and each of the four governing parameters (p_3, T_3, U_3, ER) is varied independently to provide a basic understanding of their effects on fuel burn and combustion efficiency. For the ascent case, all four variables (p_3, T_3, U_3, ER) continuously vary as the vehicle is trimmed along a constant dynamic pressure trajectory. For the ascent case, there are many competing tradeoffs that were examined.

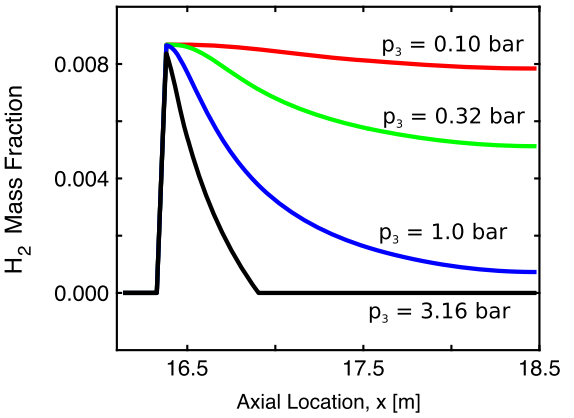

Fig. 10 Assessment case, no ascent: hydrogen mass fraction profiles for different combustor entrance pressures p_3. $T_3 = 900$ K, $U_3 = 2000$ m/s, ER $= 0.3$.

A. Assessment Case: Parameters Varied Independently

Figure 10 shows how the hydrogen fuel mass fraction varies in the axial direction within the combustor for different entrance pressures p_3. Equations (5–19) were solved for values of T_3, U_3, and ER that were fixed at 900 K, 2000 m/s, and 0.30, respectively. The hydrogen mass fraction increases sharply at $x = 16.4$ m where the fuel is injected, and then it decreases downstream due to chemical reaction. The upper curve indicates that little of the fuel is consumed at the end of the combustor ($x = 18.5$ m) when p_3 is as small as 0.1 bar. Profiles of gas static temperature and static pressure have been previously studied [6] and are not shown here; both quantities rise initially due to the heat addition from combustion and then decrease downstream due to wall divergence. Static pressure rises because heat addition to a supersonic flow drives the Mach number down (toward unity).

Figure 11 is a plot of combustion efficiencies determined for the assessment case, measured at station 4 the combustor exit. Profiles computed by solving Eqs. (5–19) were inserted into Eq. (26). As expected, higher combustion efficiency is achieved by operating at higher combustor entrance pressures and temperatures when ER is held constant. For p_3 less than 0.5 atm, a significant fraction of the hydrogen fuel is not consumed. This finding is consistent with the general understanding in Heiser et al. [10] that p_3 should exceed 0.5 atm. The trends in Fig. 11 are due to two physical processes that control hydrogen reaction rate: mixing and finite rate chemistry.

The gas velocity U_3 also was increased, and as expected, the combustion efficiency decreased because of the reduced residence time available to complete the mixing and finite rate chemistry.

The flameout limit was examined for the assessment case, and some results are shown in Fig. 12. The normalized Damköhler number was computed using Eq. (2). Figure 12a shows that reducing either the pressure p_3 or the temperature T_3, while keeping U_3 and ER constant, drives the Damköhler number down toward unity, which is the flameout limit. However, Fig. 12b also shows that increasing the equivalence ratio has a strong stabilizing effect, as expected. Propulsion devices often are operated fuel-lean, and so smaller values of ER lead to flameout at some lean limit. Larger ER conditions become closer to stoichiometric and are less likely to flame out.

B. Ascent Case: Combustor Flow Conditions

Now the ascent case is considered; it is defined by the following constraints. The trimmed MAX-1 vehicle ascends along a path of constant dynamic pressure that is selected to be either $q_\infty = 30, 50, 70,$

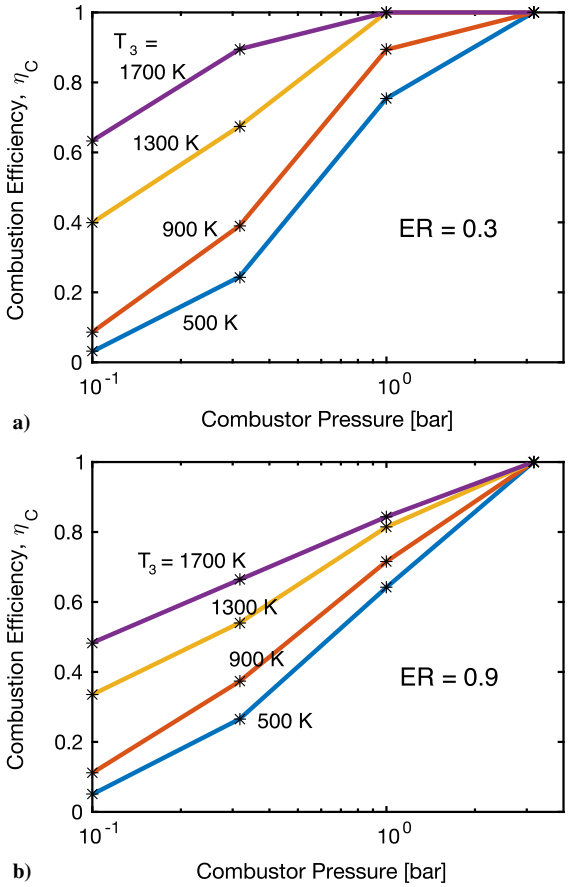

Fig. 11 Assessment case, no ascent: combustion efficiencies for a) ER = 0.3, and b) ER = 0.9. U_3 = 2000 m/s.

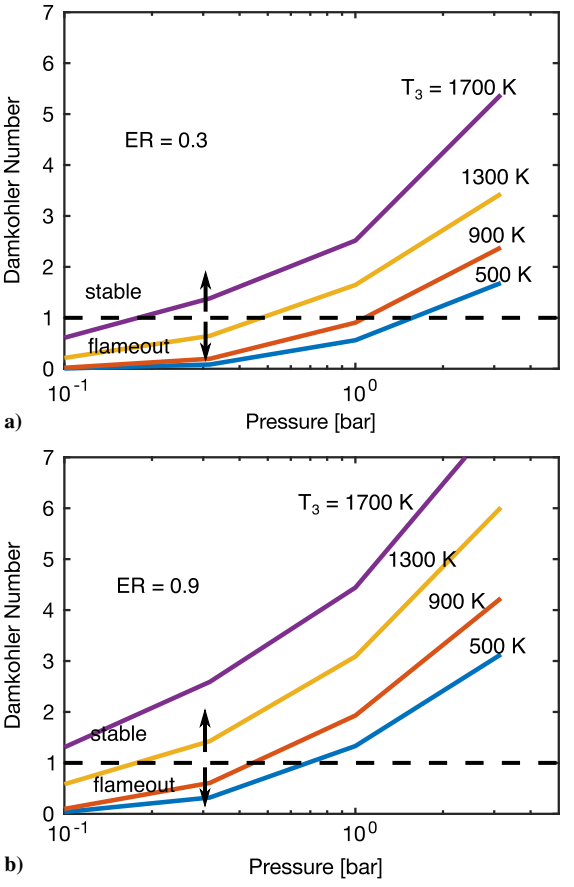

Fig. 12 Assessment case, no ascent: flameout occurs below the horizontal line $Da_H = 1$, as defined by Eq (2): a) ER = 0.30, and b) ER = 0.90. Mach number $M_3 = 2$.

or 100 kPa. Vehicle acceleration may vary along a trajectory, though in this study, $\boldsymbol{a}$ is fixed at 2 m/s^2 to reduce the dimensionality of the problem. The equivalence ratio is set by the trim requirements at this acceleration, which is low enough to prevent choking of the combustor flow and avoids ram–scram transition for all Mach numbers considered. Figure 13 shows how the four governing parameters (p_3, T_3, U_3, and ER) vary as the flight Mach number varies from 5 to 14 along several ascent trajectories (q_∞ = 30 to 300 kPa).

Combustor entrance static pressure p_3 in Fig. 13a decreases as the vehicle ascends along a trajectory. There is some expected tradeoff occurring in this case; one might expect higher Mach numbers to produce strong shocks that raise the static pressure p_3 behind them. However, along a constant q_∞ ascent trajectory M_∞ is proportional to $p_\infty^{-1/2}$, and p_∞ varies inversely with altitude (illustrated in Fig. 3). The decreasing trend of combustor pressure p_3 indicates that the atmospheric pressure conditions dominate the compression tradeoff between p_∞ and flight mach number M_∞. Also note that p_3 is not directly proportional to p_∞ because the locations of the multiple shock waves in the inlet are changing as M_∞ and the angle of attack change.

Figure 13b indicates that the static temperature at the combustor entrance (T_3) increases during the ascent. This is because the increasing flight Mach number raises the stagnation temperature and, more importantly, the Mach number M_3 of the compressed air entering the combustor, as shown in Fig. 13d. Figure 13c indicates that the entrance air velocity U_3 also increases with M_∞, primarily due to the increased speed of sound.

An important observation is that Fig. 14 shows that the equivalence ratio required to trim the vehicle increases during ascent. ER also is much larger along the small q_∞ (30 kPa) trajectory than along the 300 kPa trajectory. The trim requirement introduces interesting constraints. If a small q_∞ trajectory is selected, the vehicle flies at higher altitudes (for a certain M_∞). The ambient gas density is low, and this requires a larger angle of attack to maintain sufficient lift force. Drag tends to vary as the square of the angle of attack, and so increased thrust is needed. The low density of the ambient air means that the mass flow rate of air that is captured by the inlet decreases, which would reduce thrust unless ER is increased. Alternatively, the vehicle acceleration is fixed at 2 m/s^2, and if traveling along a high q_∞ trajectory, large amounts of air enter the engine. Thus, the ER must be reduced, as shown by the lower curve in Fig. 14.

Noticeably, we observe that, at some higher Mach numbers, the equivalence ratio rises above unity to meet the thrust requirements. This is a result of two model assumptions handling residence time and incomplete combustion. In the MASIV ROM, fuel burn only takes place in the combustor; the nozzle computations do not contain any combustion chemistry. Second, as the crossflow velocity U_3 in the combustor increases, the residence time decreases, and the flame length extends beyond the combustion chamber and out of the domain. Thus, even at a fuel–air equivalence ratio of 1, not all of the fuel may be burned, and maximum thrust attained. In such case when ER $>$ 1, a greater amount of fuel is dumped into the combustor for the opportunity to burn and produce thrust, but at the cost of reduced combustion efficiency.

C. Ascent Case: Combustion Efficiency and Flameout Limit

Figure 15 shows how combustion efficiency η_C varies during the ascent. The computed hydrogen mass fraction at the combustor exit ($Y_{H2,4}$) was inserted into Eq. (26). It can be concluded from Fig. 15 that it is advantageous to select a trajectory with a large value of dynamic pressure q_∞ to achieve high efficiency. The reason can be deduced from Fig. 13, which showed that selecting a larger dynamic pressure results in higher pressures p_3 and much lower equivalence ratios. The higher pressures tend to increase the reaction rates, and the lower ER means that the fuel is rapidly mixed because of the excess air.

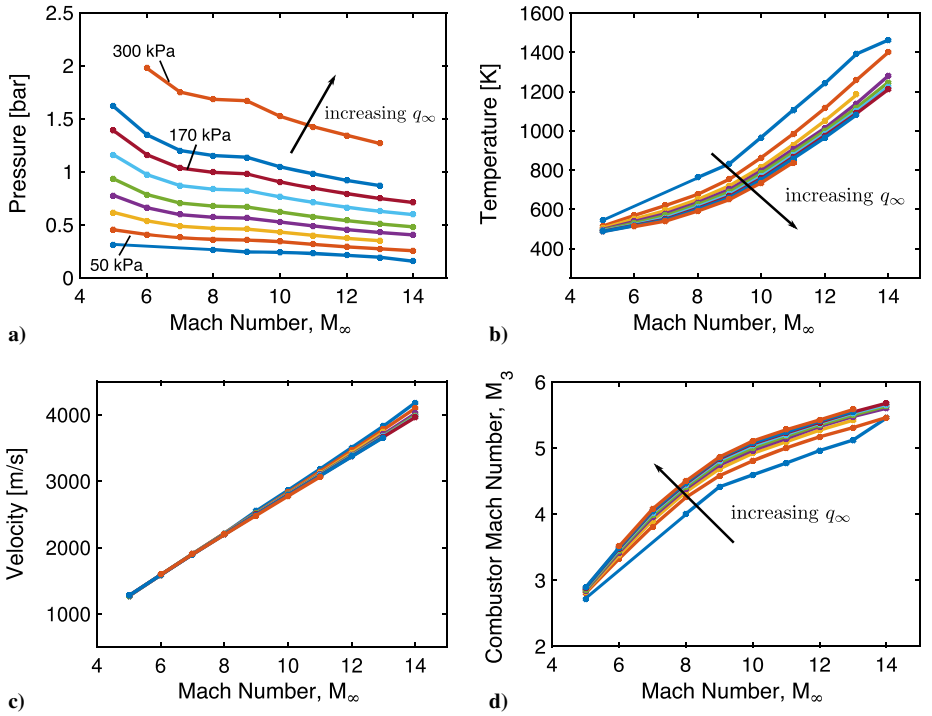

Fig. 13 Ascent case: for a dynamic pressure a) combustor entrance static pressure p_3, b) static temperature T_3, c) air velocity U_3, and d) combustor Mach number M_3 vs flight Mach number M_∞.

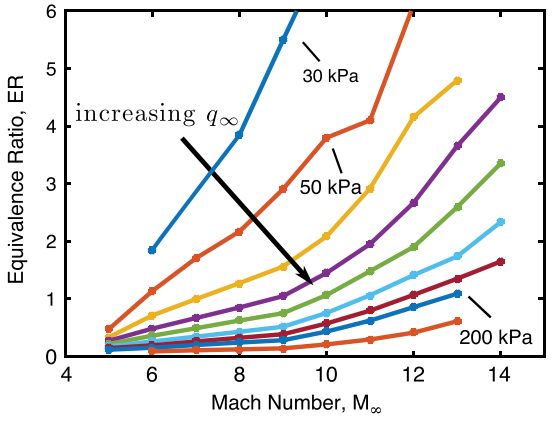

Fig. 14 Ascent case: fuel–air equivalence ratio ER vs flight Mach number, for different trajectories of constant dynamic pressure q_∞.

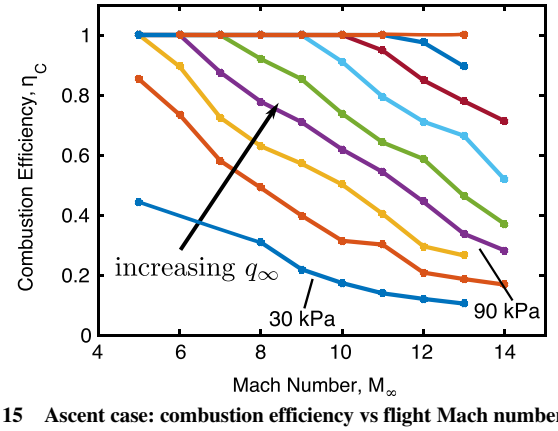

Fig. 15 Ascent case: combustion efficiency vs flight Mach number, for different trajectories of constant dynamic pressure q_∞.

A second conclusion deduced from Fig. 15 is that, for each q_∞ trajectory above some Mach number, the combustion efficiency steadily decreases during an ascent, as flight Mach number rises from 5 to 14. This appears to be due to offsetting trends in the combustor conditions. Figure 13 showed that, during the ascent, there is a decrease in p_3 and an increase in U_3, both of which tend to reduce efficiency due to slower chemistry and reduced residence time in the combustor. However, this is partially offset by the increases in T_3 and ER that are shown in Fig. 13 that tend to speed up the chemical reactions. The pressure and velocity effects dominate the chemistry processes in the combustor, and less and less of the injected fuel is burned as the vehicle accelerates, reducing the overall combustion efficiency.

The Damköhler number is plotted in Fig. 16 for two different cavity heights H. In Fig. 16b, for most of the ascent trajectories considered, Da_H exceeds unity, and so flameout is avoided. An expected result is that the lowest curve in Fig. 16 corresponds to the lowest q_∞ of 30 kPa. This means that selecting a high-dynamic-pressure, low-altitude trajectory is advantageous in avoiding flameout. A high-altitude trajectory subjects the combustor to lower static pressures and a high trimmed ER, reducing combustion efficiency and approaching critically low Damköhler numbers for a fixed step height H. A low-altitude (large q_∞) trajectory provides high pressures, and the engine entrains large amounts of air. Thus, a small (lean) ER is required by the trim conditions to prevent excessive thrust and maintain the specified 2 m/s^2 of acceleration.

Figure 16 shows that flameout occurs at high altitude (low dynamic pressure q_∞) due to a combination of low ambient pressures, reduced combustor residence time, and inefficient combustion and equivalence ratios at the target trim conditions. It is noted that a constant acceleration trajectory was studied. For ascent or cruise trajectories with a different trim constraint, it is expected that the shape and location of the flameout region will change, and a low-altitude flameout may be observed. This might correspond to a Damköhler number "rich limit" as reported in [12], whereas this study focused only on fuel lean-limit Damköhler number experiments (in Table 1). If a high-altitude trajectory is selected, Fig. 15 also shows that the combustion efficiency would be significantly decreased. In some cases, the low efficiency limit is reached before flameout occurs. For fuel, range, and overall efficiency considerations, it is desired that combustion efficiency remains high ($\eta_C > 0.90$).

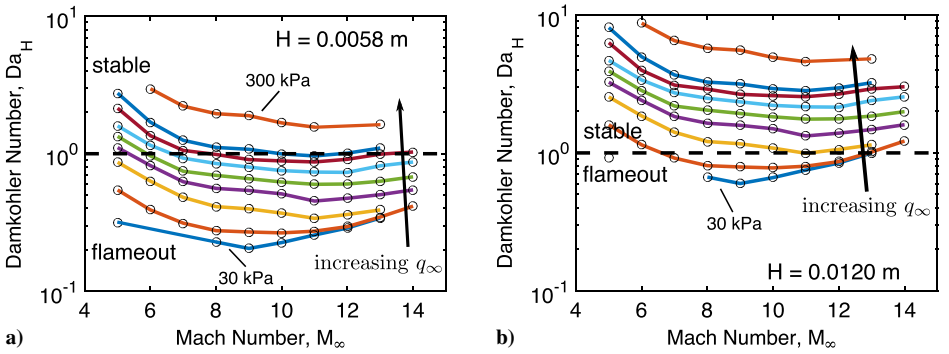

Fig. 16 Computed Damköhler number as the MAX-1 vehicle ascends along the trajectories shown in Fig. 2. Cavity height is H.

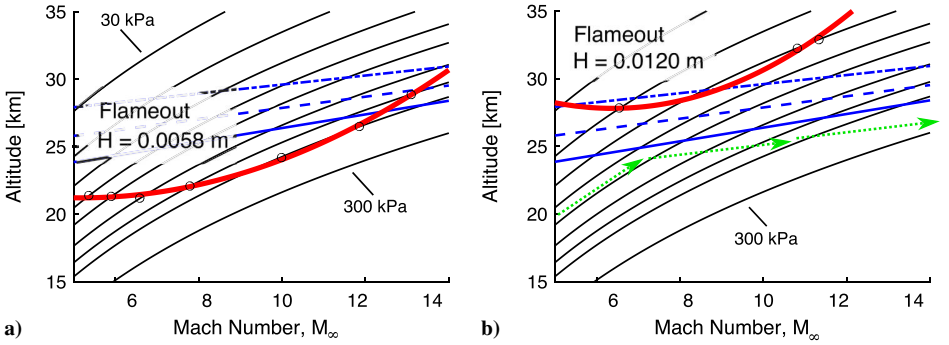

Fig. 17 Operability limits due to flameout (thickest line) and combustion efficiency exceeding 0.90 (solid line below dashed lines). Cavity height is 0.0058 m (left) and 0.0120 m (right).

D. Ascent Case: Operability Limits on a Flight Corridor Map

One goal is to plot operability limits on a flight corridor map, as seen in Fig. 17. The thin black lines represent constant dynamic pressure trajectories that relate M_∞ to altitude. The upper, curved red line in Fig. 17 is the flameout limit computed by the MASIV code. Operation above this line leads to flameout due to a combination of low pressures, reduced reaction rates, short residence times, and inefficient ER at the trim conditions. The straight, solid blue line is where the combustion efficiency is $\eta_C = 0.90$. Operation at altitudes above this line is less efficient and not desirable. The subsequent dashed blue lines represent $\eta_C = 0.75, 0.6$, respectively.

It is seen that, in Fig. 17a, only one acceptable trajectory ($q_\infty = 300$ kPa) falls outside of the curved red and solid blue lines. One alternative is to increase the flameholder step height H, which shrinks the flamout region, as seen in Fig. 17b. The flight corridor is widened, and an acceptable trajectory is shown by the green arrows. Even with a larger step height H, at higher flight Mach numbers, we approach the loose combustion efficiency limits, which tend the acceptable trajectories toward a higher q_∞.

VI. Discussion of Uncertainty

An advantage of a ROM is that it can be run rapidly for thousands of conditions to estimate trends that occur for a trimmed vehicle ascending along different trajectories. Despite uncertainties introduced by the simplifying assumptions, the computed trends provide understanding as well as multidimensional performance maps that are essential to develop optimization and control strategies. However, two disadvantages of a ROM are its limited range of applicability and the need to quantify uncertainty. The MASIV finite rate chemistry lookup tables are limited to the fuel type (hydrogen) for which they were generated. The mixture fraction (fuel mixing) profiles are limited to jets in a crossflow because they are based on empirical formulas. The flameout Damköhler number is based on an empirical number that is only valid for a cavity type of flameholder. Our methodology can be modified to account for other fuels, injectors, and flameholders, but this has not yet been done.

Uncertainties previously have been shown to be less than 15% for several of the submodels in MASIV because the selected geometry is simple. However, uncertainties are estimated to be larger for the combustor. Forces were computed using established panel methods; the angles of attack and turning angles are less than 8 deg, and so flow separation is not a concern. Panel methods were shown in [42,43] to predict pressure forces that agree with CFD results to within 10% if turning angles are less than 10 deg. The engine has a large aspect ratio of 15, and the use of the 2-D method of characteristics in the inlet and nozzle were shown in [3,6] to compute wall pressures that are within 15% of CFD and experimental results. Only a 1% uncertainty is introduced by the decision to keep only the four largest POD modes to create the smaller chemistry lookup table described in Sec. IV. A previous paper [7] focuses entirely on the uncertainties of the MASIV model.

The largest uncertainties are associated with the combustor, and they are estimated to be less than 30%. It is argued that the empirical formulas that are employed are reasonable for the simple geometry selected, but the uncertainty in the empirical constants c_1 to c_6 is about 30% due to scatter in the data from different experiments [32,33]. The MAX-1 combustor has a simple diverging duct geometry with fuel jets burning in a crossflow. Equations (12–17) are well-established mixing empirical formulas for jet mixing in a crossflow, based on experimental measurements [33]. The Damköhler number concept is commonly used [12] to correlate flame blowout data, and five sets of measurements in Table 1 yield Da^*_{crit} and k_1 values approximating blowout.

The uncertainty and variation of k_1 in some experiments is nontrivial. This provides an indication that there are further parameters beyond the Damköhler correlation of the reaction rate to the diffusion rate affecting flame stability and blowout. The exact measurement of flameout also varied between experiments, reporting either extinguished conditions or incipient flame instability as blowout. Large scatter is found in aggregate experiments using different fuels and mixing structures (cavities, struts), correlating Damköhler number to a defined equivalence ratio [12]. Quantifying the uncertainty of k_1 is difficult without further experiments;

however, in repeating the analysis of this study with a different baseline Da^*_{crit} and k_1 from Table 1, we yield the same trends of the flameout region but with a different minimum cavity step height (a tunable design parameter).

To quantify some of the uncertainty in the combustor computations, previously [4,5] compared combustor wall pressure profiles from MASIV to an experiment of identical geometry; the agreement was within 15%. Although the combustor uncertainty is larger than desired, the present empirical approach is argued to be justified because CFD codes cannot compute combustion efficiencies or flameout limits with uncertainties less than 30%. Additional measurements could reduce the uncertainty in the empirical constants c_1 to c_6 and k_1. However, the present conclusions have been limited to statements about general trends, and these conclusions are felt to be accurate.

VII. Conclusions

In this work, a methodology is presented to compute two operability limits that affect the ascent of a trimmed hypersonic vehicle that is powered by a dual-mode ramjet–scramjet engine. One is the flameout limit, and the other is the limit where combustion efficiency drops below 0.90. A reduced-order model (ROM) called MASIV was used that includes finite rate chemistry tables that are similar to those used in the code FLUENT. A 3-D turbulent mixing model uses empirical formulas for the profiles of mean fuel concentrations in jets in a crossflow. It also applies a conventional assumed-PDF approach to model turbulent mixing. A proper orthogonal decomposition (POD) algorithm was developed to reduce the size of the chemistry lookup table matrix from 93 million elements to less than 1% of this number and speed up the computation. Retaining only the largest four POD modes introduced very small inaccuracy because nearly all of the table elements that were eliminated have negligibly small values, and the original matrices were well conditioned.

Although the ROM results are only approximate, they do successfully predict several measured flameout limit trends. To determine the flameout limits the aerodynamic and thrust forces are computed approximately 1800 times. That is, for each of nine trajectories, 20 altitudes are selected. For each altitude, 10 angles of attack are selected to find the one that trims the vehicle. For this type of optimization study, a ROM gives a useful first look at the small subset of conditions that should be investigated later using CFD.

For every computation, the vehicle is trimmed at each altitude. To evaluate the model, an assessment case was run. For this case, there was no ascent, and each of the four governing variables (p_3, T_3, U_3, and ER) was systematically varied. The resulting trends were in qualitative agreement with previous experiments. For the ascent case, multidimensional maps were generated by running the MASIV model hundreds of times, through various altitudes, atmospheric conditions, angles of attack, and flight trajectories. Each trajectory has a different dynamic pressure. The variation of the angle of attack was necessary to find the trim angle and condition that balances all vehicle forces and moments at an acceleration of $\boldsymbol{a} = 2\ \text{m/s}^2$.

From the flight vehicle maps, the two operability limits were computed that define a narrow flight corridor on a plot of altitude versus flight Mach number. The optimum trajectory was identified as the one that has maximum combustion efficiency and avoids the flameout limit. Although results of the assessment case (no ascent) were straightforward, the ascent case yielded unexpected results; they arise due to competing effects of four parameters (p_3, U_3, T_3, and ER). During the ascent, the combustor entrance pressure p_3 drops, and U_3 increases, which has the adverse effect of tending to slow the chemistry and reduce the residence time. However, ascent also causes T_3 and ER to increase, which tends to speed up the chemistry. It was found that a high-altitude (low dynamic pressure) trajectory is best to avoid fuel lean-limit flameout. Although a high-altitude trajectory causes low pressures to occur the combustor, the trim requirements impose near-optimum stoichiometric fuel–air ratios that are far from the lean flameout limit.

Acknowledgments

This research was funded by the U.S. Air Force Research Laboratory/Air Vehicles Directorate grant FA8650-07-2-3744 that has supported the Michigan/AFRL Collaborative Center in Control Sciences with Michael Bolender and David Doman serving as technical monitors. The first author also has been supported by a University of Michigan Fellowship. The authors are grateful for the technical assistance provided Derek Dalle and Sean Torrez.

References

[1] Dalle, D. J., Torrez, S. M., Driscoll, J. F., Bolender, M. A., and Bowcutt, K. G., "Minimum-Fuel Ascent of a Hypersonic Vehicle Using Surrogate Optimization," *Journal of Aircraft*, Vol. 51, No. 6, 2014, pp. 1973–1986.

[2] Dalle, D. J., Driscoll, J. F., and Torrez, S. M., "Ascent Trajectories of Hypersonic Aircraft: Operability Limits Due to Engine Unstart," *Journal of Aircraft*, Vol. 52, No. 4, 2015, pp. 1345–1354. doi:10.2514/1.C032801

[3] Dalle, D. J., Fotia, M. L., and Driscoll, J. F., "Reduced-Order Modeling of Two-Dimensional Supersonic Flows with Applications to Scramjet Inlets," *Journal of Propulsion and Power*, Vol. 26, No. 3, May 2010, pp. 545–555. doi:10.2514/1.46521

[4] Torrez, S. M., Driscoll, J. F., Ihme, M., and Fotia, M. L., "Reduced-Order Modeling of Turbulent Reacting Flows with Application to Ramjets and Scramjets," *Journal of Propulsion and Power*, Vol. 27, No. 2, March 2011, pp. 371–382. doi:10.2514/1.50272

[5] Torrez, S. M., Dalle, D. J., and Driscoll, J. F., "New Method for Computing Performance of Choked Reacting Flows and Ram-to-Scram Transition," *Journal of Propulsion and Power*, Vol. 29, No. 2, March 2013, pp. 433–445. doi:10.2514/1.B34496

[6] Mbagwu, C., and Driscoll, J. F., "Operability Limits for Combustion in Air-Breathing Hypersonic Vehicles," *20th AIAA International Space Planes and Hypersonic Systems and Technologies Conference*, AIAA Paper 2015-3506, July 2015.

[7] Lamorte, N., Friedmann, P. P., Dalle, D. J., Torrez, S. M., and Driscoll, J. F., "Uncertainty Propagation in Integrated Airframe–Propulsion System Analysis for Hypersonic Vehicles," *Journal of Propulsion and Power*, Vol. 31, No. 1, Jan. 2015, pp. 54–68. doi:10.2514/1.B35122

[8] Mbagwu, C., and Driscoll, J. F., "A Method to Compute Flameout Limits of Scramjet-Powered Hypersonic Vehicles," *51st AIAA/SAE/ASEE Joint Propulsion Conference*, AIAA Paper 2015-3749, July 2015.

[9] Mbagwu, C., and Driscoll, J. F., "Flameout and Combustion Efficiency of Scramjet-Powered Hypersonic Vehicles During Ascent," *54th AIAA Aerospace Sciences Meeting*, AIAA Paper 2016-0914, Jan. 2016.

[10] Heiser, W., Pratt, D., Daley, D., and Mehta, U., *Hypersonic Airbreathing Propulsion*, AIAA, Washington, D.C., Jan. 1994, pp. 461–480.

[11] Baxter, M. R., and Lefebvre, A. H., "Flame Stabilization in High-Velocity Heterogeneous Fuel–Air Mixtures," *Journal of Propulsion and Power*, Vol. 8, No. 6, 1992, pp. 1138–1143.

[12] Driscoll, J. F., and Rasmussen, C. C., "Correlation and Analysis of Blowout Limits of Flames in High-Speed Airflows," *Journal of Propulsion and Power*, Vol. 21, No. 6, Nov. 2005, pp. 1035–1044. doi:10.2514/1.13329

[13] Ozawa, R. I., "Survey of Basic Data on Flame Stabilization and Propagation for High Speed Combustion Systems," Marquart Corp., TR AFAPL-TR-70-81, Van Nuys, CA, 1971.

[14] Shanbhogue, S. J., Husain, S., and Lieuwen, T., "Lean Blowoff of Bluff Body Stabilized Flames: Scaling and Dynamics," *Progress in Energy and Combustion Science*, Vol. 35, No. 1, 2009, pp. 98–120. doi:10.1016/j.pecs.2008.07.003

[15] Kalghatgi, G. T., "Blow-Out Stability of Gaseous Jet Diffusion Flames. Part 1: In Still Air," *Combustion Science and Technology*, Vol. 26, Nos. 5–6, Oct. 1981, pp. 233–239. doi:10.1080/00102208108946964

[16] Takahashi, S., Sato, N., Tsue, M., Kono, M., Nakamura, M., Kondo, H., and Ujiie, Y., "Control of Flame-Holding in Supersonic Airflow by Secondary Air Injection," *Journal of Propulsion and Power*, Vol. 14, No. 1, 1998, pp. 18–23. doi:10.2514/2.5260

[17] Sun, M.-B., Geng, H., Liang, J.-H., and Wang, Z.-G., "Flame Characteristics in Supersonic Combustor with Hydrogen Injection Upstream of Cavity Flameholder," *Journal of Propulsion and Power*, Vol. 24, No. 4, July 2008, pp. 688–696. doi:10.2514/1.34970

[18] Micka, D. J., and Driscoll, J. F., "Stratified Jet Flames in a Heated (1390 K) Air Cross-Flow with Autoignition," *Combustion and Flame*, Vol. 159, No. 3, March 2012, pp. 1205–1214. doi:10.1016/j.combustflame.2011.10.013

[19] Kang, S. H., Lee, Y. J., Yang, S. S., Smart, M. K., and Suraweera, M. K., "Cowl and Cavity Effects on Mixing and Combustion in Scramjet Engines," *Journal of Propulsion and Power*, Vol. 27, No. 6, Nov. 2011, pp. 1169–1177. doi:10.2514/1.48818

[20] Retaureau, G., and Menon, S., "Experimental Studies on Flame Stability of a Fueled Cavity in a Supersonic Crossflow," *46th AIAA/ASME/SAE/ASEE Joint Propulsion Conference & Exhibit*, AIAA Paper 2010-6718, July 2010.

[21] Gruber, M. R., Donbar, J. M., Carter, C. D., and Hsu, K.-Y., "Mixing and Combustion Studies Using Cavity-Based Flameholders in a Supersonic Flow," *Journal of Propulsion and Power*, Vol. 20, No. 5, 2004, pp. 769–778. doi:10.2514/1.5360

[22] Rasmussen, C. C., and Driscoll, J. F., "Characteristics of Cavity-Stabilized Flames in a Supersonic Flow," *Journal of Propulsion and Power*, Vol. 21, No. 4, 2005, pp. 765–768. doi:10.2514/1.15095

[23] Rasmussen, C. C., Driscoll, J. F., Hsu, K. Y., Donbar, J. M., Gruber, M. R., and Carter, C. D., "Stability Limits of Cavity-Stabilized Flames in Supersonic Flow," *Proceedings of the Combustion Institute*, Vol. 30, No. 2, Jan. 2005, pp. 2825–2833. doi:10.1016/j.proci.2004.08.185

[24] Rasmussen, C. C., Dhanuka, S. K., and Driscoll, J. F., "Visualization of Flameholding Mechanisms in a Supersonic Combustor Using PLIF," *Proceedings of the Combustion Institute*, Vol. 31, No. 2, Jan. 2007, pp. 2505–2512. doi:10.1016/j.proci.2006.08.007

[25] Tatman, B. J., Rockwell, R. D., Goyne, C. P., McDaniel, J. C., and Donohue, J. M., "Experimental Study of Vitiation Effects on Flameholding in a Cavity Flameholder," *Journal of Propulsion and Power*, Vol. 29, No. 2, 2013, pp. 417–423. doi:10.2514/1.B34687

[26] Bolender, M. A., and Doman, D. B., "Nonlinear Longitudinal Dynamical Model of an Air-Breathing Hypersonic Vehicle," *Journal of Spacecraft and Rockets*, Vol. 44, No. 2, 2007, pp. 374–387. doi:10.2514/1.23370

[27] O'Neill, M. K. L., and Lewis, M. J., "Design Tradeoffs on Scramjet Engine Integrated Hypersonic Waverider Vehicles," *Journal of Aircraft*, Vol. 30, No. 6, 1993, pp. 943–952. doi:10.2514/3.46438

[28] O'Brien, T. F., Starkey, R. P., and Lewis, M. J., "Quasi-One-Dimensional High-Speed Engine Model with Finite-Rate Chemistry," *Journal of Propulsion and Power*, Vol. 17, No. 6, Nov. 2001, pp. 1366–1374. doi:10.2514/2.5889

[29] Bowcutt, K. G., "Multidisciplinary Optimization of Airbreathing Hypersonic Vehicles," *Journal of Propulsion and Power*, Vol. 17, No. 6, 2001, pp. 1184–1190. doi:10.2514/2.5893

[30] Chavez, F. R., and Schmidt, D. K., "Analytical Aeropropulsive-Aeroelastic Hypersonic-Vehicle Model with Dynamic Analysis," *Journal of Guidance, Control, and Dynamics*, Vol. 17, No. 6, 1994, pp. 1308–1319. doi:10.2514/3.21349

[31] Hasselbrink, E. F., and Mungal, M. G., "Transverse Jets and Jet Flames. Part 1. Scaling Laws for Strong Transverse Jets," *Journal of Fluid Mechanics*, Vol. 443, 2001, pp. 1–25.

[32] Hasselbrink, E. F., and Mungal, M. G., "Transverse Jets and Jet Flames. Part 2. Velocity and OH Field Imaging," *Journal of Fluid Mechanics*, Vol. 443, Sept. 2001, pp. 27–68.

[33] Smith, S. H., and Mungal, M. G., "Mixing, Structure and Scaling of the Jet in Crossflow," *Journal of Fluid Mechanics*, Vol. 357, Feb. 1998, pp. 83–122. doi:10.1017/S0022112097007891

[34] Lin, K.-C., Ryan, M., Carter, C., Gruber, M., and Raffoul, C., "Raman Scattering Measurements of Gaseous Ethylene Jets in a Mach 2 Supersonic Crossflow," *Journal of Propulsion and Power*, Vol. 26, No. 3, 2010, pp. 503–513. doi:10.2514/1.43757

[35] Ihme, M., and See, Y. C., "Prediction of Autoignition in a Lifted Methane/Air Flame Using an Unsteady Flamelet/Progress Variable Model," *Combustion and Flame*, Vol. 157, No. 10, Oct. 2010, pp. 1850–1862. doi:10.1016/j.combustflame.2010.07.015

[36] Peters, N., "Laminar Diffusion Flamelet Models in Non-Premixed Turbulent Combustion," *Progress in Energy and Combustion Science*, Vol. 10, No. 3, 1984, pp. 319–339. doi:10.1016/0360-1285(84)90114-X

[37] Pitsch, H., "FLAMEMASTER V3.1: A C++ Computer Program for 0D Combustion and 1D Laminar Flame Calculations," 1998, http://web.stanford.edu/~hpitsch/FlameMaster.html [retrieved 2016].

[38] Jachimowski, C. J., "An Analytical Study of the Hydrogen–Air Reaction Mechanism with Application to Scramjet Combustion," NASA TP-2791, 1988.

[39] Hall, K. C., Thomas, J. P., and Dowell, E. H., "Proper Orthogonal Decomposition Technique for Transonic Unsteady Aerodynamic Flows," *AIAA Journal*, Vol. 38, No. 10, 2000, pp. 1853–1862. doi:10.2514/2.867

[40] Rathinam, M., and Petzold, L. R., "A New Look at Proper Orthogonal Decomposition," *SIAM Journal on Numerical Analysis*, Vol. 41, No. 5, Jan. 2003, pp. 1893–1925. doi:10.1137/S0036142901389049

[41] Cao, Y., Zhu, J., Navon, I. M., and Luo, Z., "A Reduced-Order Approach to Four-Dimensional Variational Data Assimilation Using Proper Orthogonal Decomposition," *International Journal for Numerical Methods in Fluids*, Vol. 53, No. 10, April 2007, pp. 1571–1583. doi:10.1002/(ISSN)1097-0363

[42] Allison, D., Morris, C., Schetz, J., Kapania, R., Sultan, C., Deaton, J., and Grandhi, R., "A Multidisciplinary Design Optimization Framework for Design Studies of an Efficient Supersonic Air Vehicle," *12th AIAA Aviation Technology, Integration, and Operations (ATIO) Conference and 14th AIAA/ISSMO Multidisciplinary Analysis and Optimization Conference*, AIAA Paper 2012-5492, Sept. 2012.

[43] Falcão de Campos, J. A. C., Ferreira de Sousa, P. J. A., and Bosschers, J., "A Verification Study on Low-Order Three-Dimensional Potential-Based Panel Codes," *Computers and Fluids*, Vol. 35, No. 1, Jan. 2006, pp. 61–73. doi:10.1016/j.compfluid.2004.08.002

R. D. W. Bowersox
Associate Editor